Creating and Manipulating Electron Beams in Graphene

Ming-Hao Liu (劉明豪),* Cosimo Gorini, and Klaus Richter
Institut für Theoretische Physik, Universität Regensburg, D-93040 Regensburg, Germany
(Dated: August 8, 2016)

An electron collimator composed of a point-like source and a parabolic *pn* junction is proposed as a generator of highly focused electron beams in graphene. The collimator is based on negative refraction and Klein collimation, which are unique to pseudo-relativistic Dirac materials. The electron beams generated by the lensing apparatus can be steered by a weak magnetic field without losing collimation, which makes the parabolic lens a flexible platform for next-generation graphene electron optics experiments. This is shown by a few example applications concerning angle-resolved transmission at a *pn* junction, transverse magnetic focusing, and mapping of the current flow in scanning gate microscopy.

PACS numbers: 72.80.Vp, 72.10.-d, 73.23.Ad

Ballistic charge transport of Dirac fermions has recently been an emerging hot topic in graphene electronics, thanks not only to the rapidly improving sample quality but also to the highly intertwined theoretical and experimental efforts. Accordingly, over the past few years, novel transport behaviors of electrons in single-layer graphene have been reported, such as Fabry-Pérot interference [1–3], Hofstadter butterfly in exfoliated graphene on hexagonal boron nitride (hBN) [4, 5] and in epitaxial graphene grown on hBN [6], snake states along *pn* junctions [7, 8], gate-defined electron wave guide [9, 10], negative refraction [11], ballistic Josephson junction [12, 13], transverse magnetic focusing [14–16], and imaging of their cyclotron trajectories using scanning gate microscopy [17, 18]. Although most of such experiments were done on exfoliated graphene samples, ballistic transport has also been demonstrated using CVD (chemical vapor deposition) graphene [15, 19].

Despite the stunning progress of quantum transport experiments and simulations in recent years, decent control of electron wave propagation in graphene is still limited. Whereas electrons in graphene behave like "charged photons" that exhibit both electronic and optical properties, the lack of a narrow beam source hinders the development of graphene electron optics. Motivated by the recent work on point contacts of hBN-encapsulated graphene by Handschin *et al.* [20], here we propose a simple and efficient electron collimator for point sources in graphene, exploiting negative refraction unique to Dirac materials. Contrary to Klein collimation [21] or supercollimation in superlattices [22], we consider a paraboloid *pn* junction with a point-like source located at its focal point; see Fig. 1(a).

Paraboloidals are known to have a wide variety of applications, ranging from flashlight reflectors to radiotelescope antennas [23], where either a wave emitted from a point source is turned into a plane wave by specular reflection [black arrows in Fig. 1(a)], or vice versa. For a point source of waves to *refract* toward an identical direction parallel to the parabola axis [white arrows in Fig. 1(a)], on the other hand, the refraction indices inside and outside the paraboloid must be of opposite sign, provided that the point source is located at the focal point. In graphene, the role of the refraction index is played by the Fermi energy relative to the Dirac point, and hence the carrier density relative to the charge neutrality point. Thus a paraboloidal electron lens with individually controllable inner and outer carrier densities n_i, n_o can be realized by electrical gating.

Most notably, when $n_i = -n_o$, the refracted electron waves are expected not only to collimate into a unidirectional wave, but also to concentrate in intensity in a narrow range around the parabola axis due to Klein collimation [21], i.e., the perfect

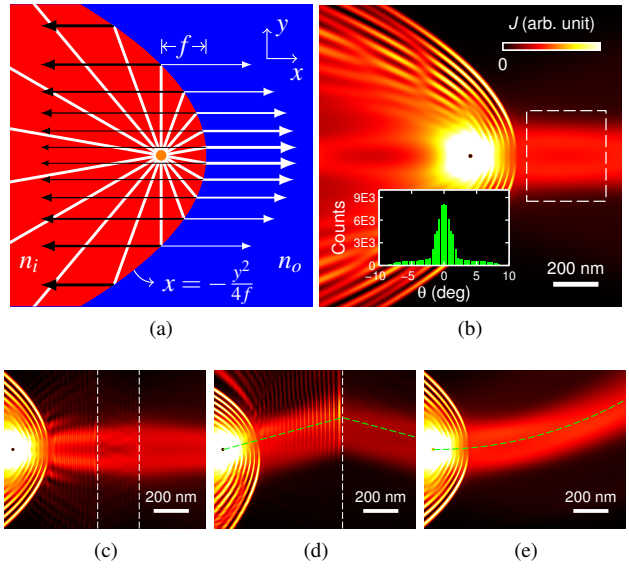

FIG. 1. (a) Schematic of the lensing apparatus composed of a point source at the focal point of a parabolic interface separating two regions with densities n_i and $n_o = -n_i$. (b) An example of the probability current density distribution due to the lensing apparatus, generating a narrow, collimated electron beam, which shows (c) nearly perfect Klein tunneling, (d) negative refraction, and (e) bending in the presence of a weak magnetic field $B = 40\,\mathrm{mT}$. Focal length $f = 200\,\mathrm{nm}$ and carrier densities $n_o = 6\times10^{11}\,\mathrm{cm}^{-2} = -n_i$ (Fermi wavelength $\approx 46\,\mathrm{nm}$) are considered in (b)–(e). Vertical white dashed lines in (c)/(d) mark an additional potential barrier/step. Green dashed lines in (d) and (e) denote the expected trajectories. Inset in (b): angle distribution (defined with respect to x-axis) of the current density analyzed for the area marked by the white dashed box.

transmission probability across the *pn* junction at normal incidence, known as the Klein tunneling [24, 25], decreases with the increasing angle of incidence. This combined effect generates a non-dispersive electron beam with width of the order of the paraboloid focal length f. This is illustrated in Fig. 1(b) by the local probability current density for $f = 200\,\mathrm{nm}$. In the rest of the paper, we refer to the parabolic *pn* junction with densities $n_i = -n_o$ combined with a point-like source at its focal point as the lensing apparatus.

The probability current density images presented are obtained by the real-space Green's function method in the tight-binding framework [26]. At site μ at (x_μ, y_μ), the local probability current density at energy E is given by the sum over the bond current vectors to the nearest neighboring sites,

$$\mathbf{J}(E; x_\mu, y_\mu) = \sum_{\nu \in \text{n.n.}} J_{\mu\to\nu}(E)\mathbf{e}_{\mu\to\nu} \,, \tag{1}$$

where $\mathbf{e}_{\mu\to\nu}$ is the unit vector pointing from μ to ν, and

$$J_{\mu\to\nu}(E) = \frac{v_F}{4\pi S}[G^<_{\mu,\nu}(E) - G^<_{\nu,\mu}(E)] \tag{2}$$

can be expressed in terms of the Keldysh Green's function matrix $G^<$. In noninteracting systems, with the incoming wave sent from one single lead described by self-energy Σ_i, the Keldysh Green's function is given by the kinetic equation $G^<(E) = G^r(E)[\Sigma_i^\dagger(E) - \Sigma_i(E)]G^a(E)$, where $G^{r/a}$ is the retarded/advanced Green's function of the scattering region.

To treat micron-scale graphene samples, we use the scalable tight-binding model for graphene [27], and adopt a scaling factor $s_f = 8$. This scales the lattice spacing to $a \sim 1\,\mathrm{nm}$, enabling us to treat (i) the density range of the order of $10^{12}\,\mathrm{cm}^{-2}$, typical for experiments using hBN-encapsulated graphene [28], and (ii) a sharp *pn* interface of smoothness $\sim 30\,\mathrm{nm} \gg a$, typical thickness of hBN encapsulation layers. Note that the prefactor in Eq. (2) containing the Fermi velocity v_F and the unit area $S = 3\sqrt{3}a^2/4$ is irrelevant for current density imaging since only dimensionless profiles are shown. In our simulations, the diameter of the point-like injector [29] will be fixed as 25 nm for convenience, which is not too far from the present technical limit [20].

The local current density profiles shown in this work refer to the magnitude $J(x,y) = [J_x^2(x,y) + J_y^2(x,y)]^{1/2}$ of Eq. (1), with the Fermi energy set to $E = 0$ and the on-site energy profiles obtained from the carrier density profiles described in Ref. 27. To further quantify the degree of electron beam collimation depicted in Fig. 1(b), the inset shows the angle distribution histogram of the azimuthal angle $\theta = \arg[J_x(x_\mu, y_\mu) + iJ_y(x_\mu, y_\mu)]$ for sites μ within the area marked by the white dashed box (with totally 80800 sites). The peak width of the angle distribution, as narrow as $\sim 5^\circ$, shows a highly collimated electron beam.

The gallery of panels Fig. 1(c)–1(e) demonstrates various properties of the focused electron beam: In Fig. 1(c), an additional barrier (marked by the white dashed lines) with density gated to $-n_o$ is considered. The collimated beam tunnels through the barrier almost reflectionlessly, a consequence of

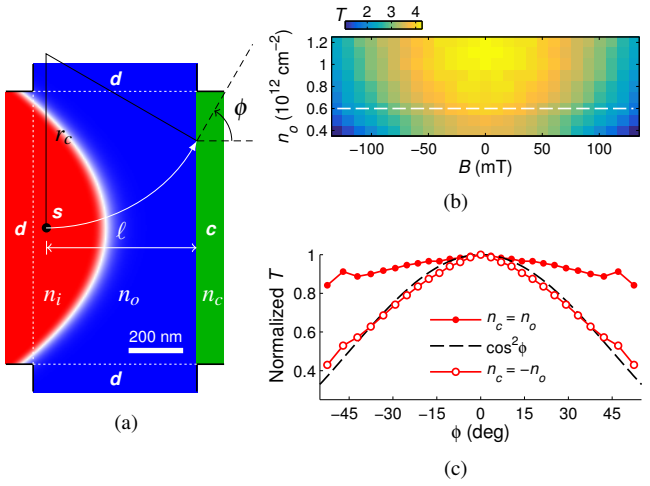

FIG. 2. (a) Schematic of the lensing apparatus in the presence of a weak magnetic B field. (b) Transmission T for electron flow from the point source (s) to the collector (c) as a function of field strength and density n_o outside the lens. The density inside the lens is set to $n_i = -n_o$, and the density in the collector lead is fixed at $n_c = -6\times10^{11}\,\mathrm{cm}^{-2}$. Along the white dashed line, $T(B)$ normalized to its maximum is re-interpreted as $T(\phi)$ in (c), with $\phi(B)$ given by Eq. (3), and compared to $\cos^2\phi$ (black dashed curve). As a reference curve, $T(\phi)$ with $n_c = n_o$ is also shown.

Klein tunneling. In Fig. 1(d), an additional potential step (to the right of the white dashed line) with density gated to $-n_o$ results in a symmetrically and negatively refracted electron beam which is clearly visible from the current density; the green dashed line marks the expected trajectory in the ray optical limit. The collimation generated by the lensing apparatus also works in the presence of a weak perpendicular magnetic field, $\mathbf{B} = (0,0,B)$, where "weak" means that the resulting cyclotron radius $r_c = \hbar\sqrt{\pi|n_o|}/eB \gg f$. This is clearly seen in Fig. 1(e), where the green dashed line marks the expected cyclotron trajectory segment.

This fact that the electron beam can be bent by a B field without losing collimation enables one to accurately measure the angle-resolved transmission of electrons traversing a *pn* junction, which has remained an experimental challenge despite some recent efforts [30, 31]. Using the proposed lensing apparatus, the angle of incidence can be continuously varied by tuning the B field, which bends the electron beam to a cyclotron trajectory segment. To simulate such an angle-resolved transmission "experiment", we perform a transport calculation considering the geometry in Fig. 2(a). There, the transparent drain leads labeled by d are to suppress boundary effects from the finite-size graphene lattice. After traversing a distance ℓ along the parabola axis, a bent trajectory hits the interface under an angle (with respect to its normal)

$$\phi = \arcsin\frac{eB\ell}{\hbar\sqrt{\pi|n_o|}} \,, \tag{3}$$

which can be controlled by the field strength B and density n_o.

Figure 2(b) shows the transmission T for charge flow from

the source s to the collector c as a function of magnetic field B and density n_o by varying the density inside the lens $n_i = -n_o$ accordingly and fixing $n_c = -6\times10^{11}\,\mathrm{cm}^{-2}$ at the collector. $T(\phi)$ in Fig. 2(c) is obtained by taking $T(B)$ along the white dashed line cut in Fig. 2(b) and using $\phi(B)$ given by Eq. (3). Since along this line cut the sharp pn junction between the scattering region and the collector lead becomes symmetric ($n_o = -n_c$), the transmission function is expected to behave like a cosine squared [21]. As seen in Fig. 2(c), the normalized $T(\phi)$ indeed agrees well with $\cos^2\phi$. As a reference line, $T(\phi)$ for $n_c = n_o = 6\times10^{11}\,\mathrm{cm}^{-2}$ is also shown in Fig. 2(c), which reasonably exhibits a nearly ϕ-independent form. Due to the spatial limit of the considered geometry, both $T(\phi)$ curves with $n_c = -n_o$ and $n_c = n_o$ exhibit a small kink around $\phi \approx \pm45^\circ$, which is simply a boundary effect. By either shortening ℓ or increasing the width, it is possible to investigate $T(\phi)$ up to higher angles.

Bending the electron beam in a controllable way makes it also particularly suitable for transverse magnetic focusing (TMF). Very recently, TMF in high-mobility graphene has gained strong experimental interest [14–18] as a tool to study and engineer charge carrier flow. TMF requires that the carrier density fulfills

$$n = \frac{1}{\pi}\left(\frac{eB}{h}\frac{D}{j}\right)^2, \qquad (4)$$

where j is a positive integer and D is the distance between the midpoints of a source and a collector probe. Here we consider a 2-μm-wide graphene sample [see left inset in Fig. 3(a)] with the right side attached to a transparent lead (d), such that the sample becomes semi-infinite, and the left side attached to two probes of width $w = 0.4\,\mu$m, one source (s) and one collector (c), separated by $D = 1.6\,\mu$m from each other. We consider only transmission from s to c for a two-point measurement, instead of all the six conductance coefficients required for the four-point resistance using Büttiker formula [26].

For fixed density $n = 6\times10^{11}\,\mathrm{cm}^{-2}$, the normalized transmission $T(B)$ is shown by the black curve with open circles in Fig. 3(a), with two broad peaks corresponding to $j = 1$ and $j = 2$ in line with Eq. (4). Replacing the probe s by the lensing apparatus with $f = 100\,$nm [right inset of Fig. 3(a)], the normalized $T(B)$ is shown by the red curve with solid dots in Fig. 3(a). The lensing apparatus clearly sharpens the TMF signal by narrowing down the peak width for $j = 1$. Most notably, outside the peak, $T(B)$ drops drastically to zero, implying a well defined, curved electron beam. In fact, the first TMF peak with lensing occurs roughly between $B = 0.1\,$T and $B = 0.13\,$T, which corresponds to cyclotron diameters of $2r_c \approx 1.81\,\mu$m and $2r_c \approx 1.39\,\mu$m, respectively, and the difference $\approx 0.42\,\mu$m agrees well with the collector probe width of $w = 0.4\,\mu$m, again suggesting a highly concentrated electron beam. In Figs. 3(b)/3(c), we show $T(B,n)$ color maps without/with the lensing apparatus; the latter clearly exhibits enhanced $j = 1,2$ TMF peaks.

Finally, we move on to the last example: the scanning gate microscopy (SGM). In SGM experiments, a capacitively coupled charged tip is scanned over a phase-coherent sample, thus acting as a tunable and movable scatterer, and the sample conductance (or resistance in four-point measurements) is measured as a function of the tip position $\mathbf{r}_{\mathrm{tip}}$. The difference $\Delta G(\mathbf{r}_{\mathrm{tip}}) \equiv G(\mathbf{r}_{\mathrm{tip}}) - G_0$ between the sample conductance with (G) and without (G_0) the tip is plotted as a function of $\mathbf{r}_{\mathrm{tip}}$. The images thus obtained were originally interpreted as maps of the coherent electron flow through quantum point contacts defined in two-dimensional electron gases (2DEGs) [32]: Backscattering from the tip in a region where a lot of electrons are passing by will cause a sizeable conductance change, the contrary holding true when the tip is positioned away from such "high flow" regions.

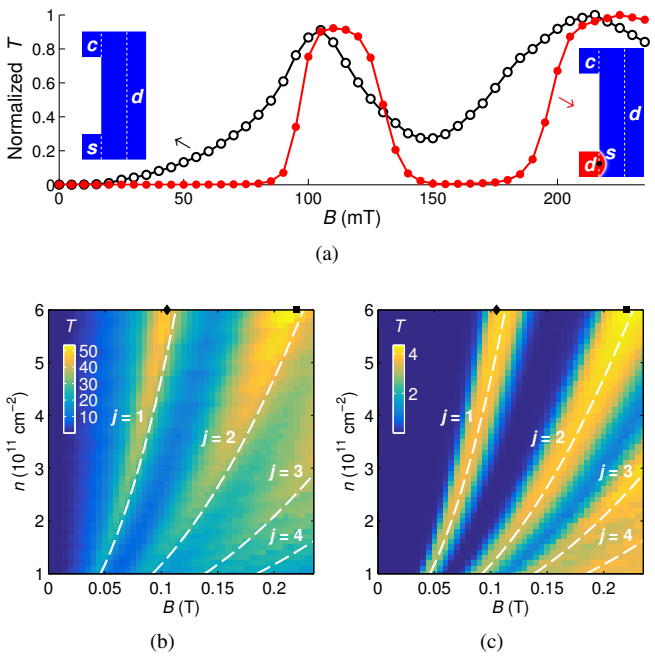

FIG. 3. Transverse magnetic focusing (TMF). (a) Normalized transmission T from source s to collector c as a function of B at density $n = 6\times10^{11}\,\mathrm{cm}^{-2}$ in the TMF geometry, without (left inset, black curve) and with (right inset, red curve) the lensing apparatus [similar to Fig. 2(a)] at lower left terminal. (b)/(c) Color maps of transmission $T(B,n)$ (not normalized) without/with the lensing apparatus. TMF states for $j = 1,\ldots,4$ predicted by Eq. (4) are marked by white dashed lines. Values of B and n marked by ♦ and ■ in (b)/(c) correspond to Fig. 4(a)/4(c) and Fig. 4(b)/4(d), respectively.

Previous theoretical and experimental works considering a variety of phase-coherent systems [33–45] showed the versatility of this technique, but also that a general interpretation of an SGM image as a flow map can be problematic [36, 37, 40, 41]. In particular, it was shown in Refs. 37 and 40 that an explicit connection between local current densities and SGM images requires stringent symmetry conditions. This is consistent with measurements in 2DEGs mesoscopic rings [35, 36], which established a connection between the local density of states and the ΔG images, as well as with recent theoretical [42] and experimental [41] developments.

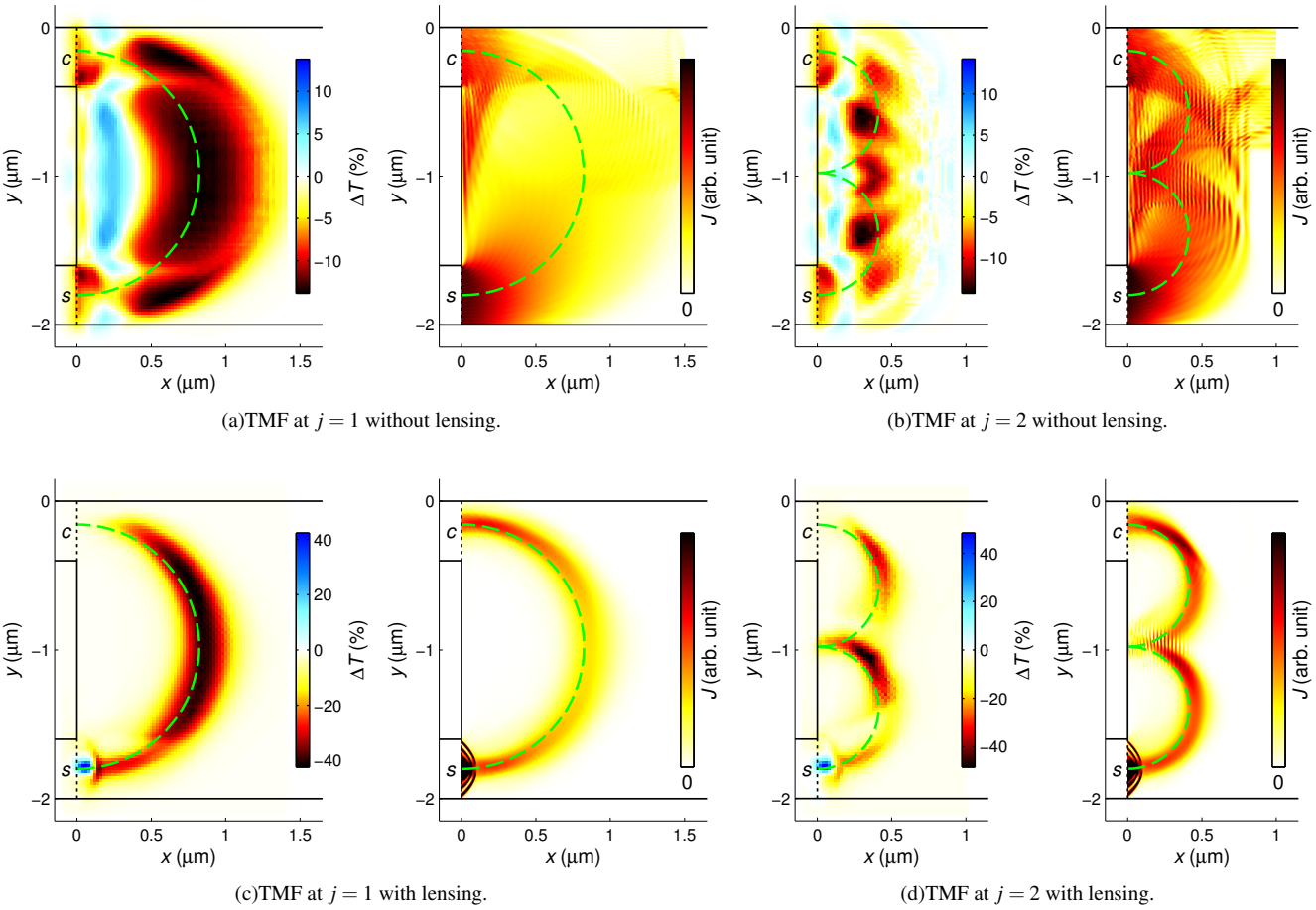

(a)TMF at $j = 1$ without lensing.

(b)TMF at $j = 2$ without lensing.

(c)TMF at $j = 1$ with lensing.

(d)TMF at $j = 2$ with lensing.

FIG. 4. Scanning gate images $\Delta T(x,y)$ versus the probability current density distribution $J(x,y)$ without/with the lensing apparatus for (a)/(c) $j = 1$ and (b)/(d) $j = 2$ TMF states, respectively, with magnetic field B and carrier density n marked by the solid diamond and solid square in Fig. 3(b)/3(c). Green dashed lines in each panel denote the expected classical trajectories in a ray picture.

In this context, the lensing apparatus is an ideal tool for testing the interpretation of SGM measurements. For the TMF geometry considered in Fig. 3 we compare in Fig. 4 the calculated SGM images ΔT and probability current density maps $J(x,y)$, without [Figs. 4(a)–4(b)] and with [Figs. 4(c)–4(d)] the lensing apparatus. Here, $\Delta T(x,y) = T(x,y) - T_0$, where T_0 without the perturbing tip has been shown in Figs. 3(b)–3(c) and $T(x,y)$ is the transmission function from s to c in the presence of a tip at $\mathbf{r}_{\rm tip} = (x,y)$ inducing a local carrier density change modeled by $n_{\rm tip}(x,y) = n^0_{\rm tip} h^3 (x^2 + y^2 + h^2)^{-3/2}$ with $n^0_{\rm tip} = -5 \times 10^{11}\,{\rm cm}^{-2}$ and $h = 50\,{\rm nm}$ adopted from Ref. 18.

Our three-terminal sample does not meet any particular symmetry requirement, and therefore we do not expect a clear correlation between the local current densities and the SGM maps [40]. This is confirmed by Figs. 4(a) and 4(b): electrons injected into the system generate complex current patterns extending over most of the sample [right panels of Figs. 4(a) and 4(b)], which are barely reflected by the SGM images – note that the latter agree with recent measurements on graphene [17, 18]. The lensing apparatus drastically changes the picture. In the right panels of Figs. 4(c) and 4(d) the current densities focus as narrow beams and agree very well with the expected classical trajectories marked by green dashed lines, in sharp contrast to the case without the lensing apparatus [Figs. 4(a)–4(b)]. Moreover, the SGM maps in the presence of the lensing apparatus [left panels of Figs. 4(c) and 4(d)] also show a highly concentrated beam structure that agrees well with the classical trajectories. In other words, the SGM signal and the local current density carry the same information. As a consequence, the system response to the local tip perturbation can be unambiguously interpreted classically in terms of the local current flow.

In conclusion, the proposed lensing apparatus for graphene has been shown to generate highly collimated, non-dispersive electron beams, which can be steered by a weak magnetic field without losing collimation. As the underlying mechanism exploits negative refraction and Klein collimation that are unique to pseudo-relativistic Dirac materials, the lensing mechanism may equally apply to topological insulators. Our lens allows unprecedented control over the electron propagation in ballistic graphene, as demonstrated by the example ap-

plications of angle-resolved transmission across a *pn* junction, transverse magnetic focusing, and imaging of the current flow using scanning gate microscopy. We expect to excite next-generation graphene electron optics experiments based on the proposed parabolic lens.

We thank P. Rickhaus, P. Makk, and C. Handschin for sharing their opinion about experimental feasibility. Financial support by DFG within SFB 689 is gratefully acknowledged.

* minghao.liu.taiwan@gmail.com

[1] A. F. Young and P. Kim, Nat. Phys. **5**, 222 (2009).
[2] P. Rickhaus, R. Maurand, M.-H. Liu, M. Weiss, K. Richter, and C. Schönenberger, Nat. Commun. **4**, 2342 (2013).
[3] A. L. Grushina, D.-K. Ki, and A. F. Morpurgo, Appl. Phys. Lett. **102**, 223102 (2013).
[4] L. Ponomarenko, R. Gorbachev, G. Yu, D. Elias, R. Jalil, A. Patel, A. Mishchenko, A. Mayorov, C. Woods, J. Wallbank, *et al.*, Nature **497**, 594 (2013).
[5] C. Dean, L. Wang, P. Maher, C. Forsythe, F. Ghahari, Y. Gao, J. Katoch, M. Ishigami, P. Moon, M. Koshino, *et al.*, Nature **497**, 598 (2013).
[6] W. Yang, X. Lu, G. Chen, S. Wu, G. Xie, M. Cheng, D. Wang, R. Yang, D. Shi, K. Watanabe, T. Taniguchi, C. Voisin, B. Plaçais, Y. Zhang, and G. Zhang, Nano Lett. **16**, 2387 (2016).
[7] T. Taychatanapat, J. Y. Tan, Y. Yeo, K. Watanabe, T. Taniguchi, and B. Özyilmaz, Nat. Commun. **6**, 6093 (2015).
[8] P. Rickhaus, P. Makk, M.-H. Liu, E. Tóvári, M. Weiss, R. Maurand, K. Richter, and C. Schönenberger, Nat. Commun. **6**, 6470 (2015).
[9] P. Rickhaus, M.-H. Liu, P. Makk, R. Maurand, S. Hess, S. Zihlmann, M. Weiss, K. Richter, and C. Schönenberger, Nano Lett. **15**, 5819 (2015).
[10] M. Kim, J.-H. Choi, S.-H. Lee, K. Watanabe, T. Taniguchi, S.-H. Jhi, and H.-J. Lee, Nat. Phys. , advance online publication (2016).
[11] G.-H. Lee, G.-H. Park, and H.-J. Lee, Nat. Phys. **11**, 925 (2015).
[12] V. E. Calado, S. Goswami, G. Nanda, M. Diez, A. R. Akhmerov, K. Watanabe, T. Taniguchi, T. M. Klapwijk, and L. M. K. Vandersypen, Nat. Nano. **10**, 761 (2015).
[13] M. B. Shalom, M. J. Zhu, V. I. Fal'ko, A. Mishchenko, A. V. Kretinin, K. S. Novoselov, C. R. Woods, K. Watanabe, T. Taniguchi, A. K. Geim, and J. R. Prance, Nat. Phys. **12**, 318 (2016).
[14] T. Taychatanapat, K. Watanabe, T. Taniguchi, and P. Jarillo-Herrero, Nat. Phys. **9**, 225 (2013).
[15] V. E. Calado, S.-E. Zhu, S. Goswami, Q. Xu, K. Watanabe, T. Taniguchi, G. C. A. M. Janssen, and L. M. K. Vandersypen, Appl. Phys. Lett. **104**, 023103 (2014).
[16] M. Lee, J. R. Wallbank, P. Gallagher, K. Watanabe, T. Taniguchi, V. I. Fal'ko, and D. Goldhaber-Gordon, ArXiv e-prints (2016), arXiv:1603.01260 [cond-mat.mes-hall].
[17] S. Morikawa, Z. Dou, S.-W. Wang, C. G. Smith, K. Watanabe, T. Taniguchi, S. Masubuchi, T. Machida, and M. R. Connolly, Appl. Phys. Lett. **107**, 243102 (2015).
[18] S. Bhandari, G.-H. Lee, A. Klales, K. Watanabe, T. Taniguchi, E. Heller, P. Kim, and R. M. Westervelt, Nano Lett. **16**, 1690 (2016).
[19] L. Banszerus, M. Schmitz, S. Engels, M. Goldsche, K. Watanabe, T. Taniguchi, B. Beschoten, and C. Stampfer, Nano Letters **16**, 1387 (2016).
[20] C. Handschin, B. Fülöp, P. Makk, S. Blanter, M. Weiss, K. Watanabe, T. Taniguchi, S. Csonka, and C. Schönenberger, Appl. Phys. Lett. **107**, 183108 (2015).
[21] V. V. Cheianov and V. I. Fal'ko, Phys. Rev. B **74**, 041403 (2006).
[22] C.-H. Park, Y.-W. Son, L. Yang, M. L. Cohen, and S. G. Louie, Nano Lett. **8**, 2920 (2008).
[23] E. Hecht, *Optics* (Pearson Education, 2015).
[24] O. Klein, Zeitschrift für Physik **53**, 157 (1929).
[25] M. I. Katsnelson, K. S. Novoselov, and A. K. Geim, Nat. Phys. **2**, 620 (2006).
[26] S. Datta, *Electronic Transport in Mesoscopic Systems* (Cambridge University Press, Cambridge, 1995).
[27] M.-H. Liu, P. Rickhaus, P. Makk, E. Tóvári, R. Maurand, F. Tkatschenko, M. Weiss, C. Schönenberger, and K. Richter, Phys. Rev. Lett. **114**, 036601 (2015).
[28] C. R. Dean, A. F. Young, I. Meric, C. Lee, L. Wang, S. Sorgenfrei, K. Watanabe, T. Taniguchi, P. Kim, K. L. Shepard, and J. Hone, Nat. Nano. **5**, 722 (2010).
[29] The point-like injector is modeled by a self-energy calculated using (i) the cell Hamiltonian H_0 belonging to the block of the N_d sites within the defined disk area of the full Hamiltonian of the considered scaled graphene lattice, and (ii) the hopping Hamiltonian H_{+1} given by an $N_d \times N_d$ identity matrix multiplied by $-t$. For the disk diameter of 25 nm considered in all numerical examples of the present work using $s_f = 8$ scaled graphene, $N_d = 258$.
[30] S. Sutar, E. S. Comfort, J. Liu, T. Taniguchi, K. Watanabe, and J. U. Lee, Nano Lett. **12**, 4460 (2012).
[31] A. Rahman, J. W. Guikema, N. M. Hassan, and N. Marković, Appl. Phys. Lett. **106**, 013112 (2015).
[32] M. A. Topinka, B. J. LeRoy, R. M. Westervelt, S. E. J. Shaw, R. Fleischmann, E. J. Heller, K. D. Maranowski, and A. C. Gossard, Nature **410**, 183 (2001).
[33] M. T. Woodside and P. L. McEuen, Science **296**, 1098 (2002).
[34] K. E. Aidala, R. E. Parrott, T. Kramer, E. Heller, R. Westervelt, M. P. Hanson, and A. C. Gossard, Nat. Phys. **3**, 464 (2007).
[35] F. Martins, B. Hackens, M. G. Pala, T. Ouisse, H. Sellier, X. Wallart, S. Bollaert, A. Cappy, J. Chevrier, V. Bayot, and S. Huant, Phys. Rev. Lett. **99**, 136807 (2007).
[36] M. G. Pala, B. Hackens, F. Martins, H. Sellier, V. Bayot, S. Huant, and T. Ouisse, Phys. Rev. B **77**, 125310 (2008).
[37] R. A. Jalabert, W. Szewc, S. Tomsovic, and D. Weinmann, Phys. Rev. Lett. **105**, 166802 (2010).
[38] S. Schnez, J. Güttinger, C. Stampfer, K. Ensslin, and T. Ihn, New J. Phys. **13**, 053013 (2011).
[39] N. Paradiso, S. Heun, S. Roddaro, L. Sorba, F. Beltram, G. Biasiol, L. N. Pfeiffer, and K. W. West, Phys. Rev. Lett. **108**, 246801 (2012).
[40] C. Gorini, R. A. Jalabert, W. Szewc, S. Tomsovic, and D. Weinmann, Phys. Rev. B **88**, 035406 (2013).
[41] A. A. Kozikov, D. Weinmann, C. Rössler, T. Ihn, K. Ensslin, C. Reichl, and W. Wegscheider, New J. Phys. **15**, 083005 (2013).
[42] K. Kolasiński and B. Szafran, New J. Phys. **16**, 053044 (2014).
[43] N. Aoki, C. R. da Cunha, R. Akis, D. K. Ferry, and Y. Ochiai, J. Phys: Condens. Matter **26**, 193202 (2014).
[44] A. A. Zhukov, C. Volk, A. Winden, H. Hardtdegen, and T. Schäpers, J. Phys.: Condens. Matter **26**, 165304 (2014).
[45] A. Kleshchonok, G. Fleury, J.-L. Pichard, and G. Lemarié, Phys. Rev. B **91**, 125416 (2015).